INTERNATIONAL JOURNAL FOR NUMERICAL METHODS IN FLUIDS
Int. J. Numer. Meth. Fluids 2001; **36**: 597–617 (DOI: 10.1002/fld.147)

Numerical computations of supersonic inlet flow

S. S. Gokhale* and Venkat Ramana Kumar

Department of Aerospace Engineering, IIT Madras, Chennai, India

SUMMARY

Air-breathing propulsion systems for high-speed space travel applications are studied. Ramjets and scramjets have been identified as potential candidates. The flow inlets of such systems are modelled with a simulation that can predict all complex inlet flow features, including shock due to forebody, multiple shock reflections, normal shock, shock–boundary layer interaction and associated separation for two-dimensional and axisymmetric inlets. Computed values are in good agreement with experimental data. Copyright © 2001 John Wiley & Sons, Ltd.

KEY WORDS: mass flow rate; numerical simulation; shock–boundary layer interaction; supersonic inlet flow

1. INTRODUCTION

Flow in inlets of supersonic air-breathing propulsion systems possesses several characteristic features that make experimental investigation a challenging and often a difficult task. Experimental investigations can highlight gross parameters, such as pressure recovery, mass flow rates, approximate shock location, etc. However, in order to find the finer details, features such as flow reversal and separation, shock–boundary layer interactions and shock reflection, one needs to resort to detailed numerical simulation.

Air-breathing propulsion systems for high-speed space application are currently studied with renewed interest. These futuristic space vehicles are manoeuvrable requiring no special launch platforms, are reusable and produce a high specific impulse compared to the conventional solid or liquid rockets, as they utilize the atmospheric oxygen for combustion. Ramjets and scramjets have been identified as potential candidates for the high-speed propulsion. Ramjets are preferred engines for flight in the Mach number range of 2–5, whereas scramjets are well suited for hypersonic speeds. The compression of air entering the intake is accomplished by decelerating the air stream. This could be achieved in several steps, such as passing through one or more oblique shocks generated due to forebody of inlet, decelerating the supersonic

---

* Correspondence to: Department of Aerospace Engineering, Indian Institute of Technology Madras, Chennai-600 036, India.

Received September 1999
Revised February 2000

flow in the convergent duct, transforming the supersonic flow into a subsonic flow through an oblique or oblique–normal shock wave system. When the flight Mach number exceeds 4, decelerating the flow to subsonic speed is particularly disadvantageous. Excessive performance loss in terms of pressure recovery due to the normal shock wave system, excessive wall heat transfer rates and combustion conditions that lose a large fraction of the available chemical energy due to dissociation are some of the problems that need to be addressed. A solution to this problem is to only partially decelerate the incoming air and avoid the normal shock wave, which may result in burner entry Mach number being supersonic.

In this context, the main objective of air intake design for the air-breathing engines is to ensure the adequate air supply to engine with minimum losses under all operating conditions. The characteristics of the supersonic inlet flow field are dominated by the shock wave system, reflected shocks as well as shock–boundary layer interactions, which must be considered essential for the design of intakes.

2. GOVERNING EQUATIONS

Earlier work carried out in internal flows at IIT Madras by Gokhale *et al.* [1] was for two-dimensional and axisymmetric nozzles. With the help of algebraic grid clustering and a simple Baldwin–Lomax model for turbulence, quantitatively accurate results, which compared well with experimental data, were obtained for isoenthalpic flows in favourable pressure gradient conditions. A similar methodology was adopted for the present work. The compressible Navier–Stokes equations in two dimensions without body force or external heat addition are taken as the governing equations. These equations are in strong conservative form for two-dimensional flows and in quasi-conservative form for axisymmetric flows. They are written as

$$\frac{\partial U}{\partial t}+\frac{\partial F}{\partial x}+\frac{\partial G}{\partial y}+H=0$$

where

$$U=\begin{bmatrix}\rho\\ \rho u\\ \rho v\\ E_t\end{bmatrix},\qquad F=\begin{bmatrix}\rho u\\ \rho u^2+p-\tau_{xx}\\ \rho uv-\tau_{xy}\\ (E_t+p)u-u\tau_{xx}-v\tau_{xy}+q_x\end{bmatrix}$$

$$G=\begin{bmatrix}\rho v\\ \rho uv-\tau_{xy}\\ \rho v^2+p-\tau_{yy}\\ (E_t+p)v-u\tau_{xy}-v\tau_{yy}+q_y\end{bmatrix}$$

and

$$H=\frac{I}{y}\begin{bmatrix} \rho v \\ \rho uv-\tau_{xy} \\ \rho v^2-(\tau_{yy}-\tau_{\theta\theta}) \\ (E_t+p)v-(u\tau_{xy}+v\tau_{yy}-q_y) \end{bmatrix}$$

$I=0$ for two-dimensional flows; $I=1$ for axisymmetric flows

$$E_t=\rho\left(C_vT+\frac{1}{2}(u^2+v^2)\right), \qquad p=\rho RT$$

$$\tau_{xx}=2\mu\frac{\partial u}{\partial x}-\frac{2}{3}\mu\nabla\cdot\vec{V}, \qquad \tau_{yy}=2\mu\frac{\partial v}{\partial y}-\frac{2}{3}\mu\nabla\cdot\vec{V}$$

$$\tau_{\theta\theta}=2\mu\frac{v}{y}-\frac{2}{3}\mu\nabla\cdot\vec{V}, \qquad \tau_{xy}=\mu\left(\frac{\partial v}{\partial x}+\frac{\partial u}{\partial y}\right)$$

$$q_x=-k\frac{\partial T}{\partial x}, \qquad q_y=-k\frac{\partial T}{\partial y}$$

$$\nabla\cdot\vec{V}=\begin{cases} \dfrac{\partial u}{\partial x}+\dfrac{\partial v}{\partial y} & \text{for two-dimensional flow} \\ \dfrac{\partial u}{\partial x}+\dfrac{1}{y}\dfrac{\partial (yv)}{\partial y} & \text{for axisymmetric flow} \end{cases}$$

The molecular viscosity coefficient μ is obtained from Sutherland's law and the coefficient of thermal conductivity k is obtained from the expression for the Prandtl number

$$\mu=\mu_l+\mu_t \quad \text{and} \quad k=\left(\frac{\mu_l}{Pr_l}+\frac{\mu_t}{Pr_t}\right)c_p$$

3. TURBULENCE MODELLING

The Baldwin–Lomax turbulence model is used in the governing equations to simulate the effects of fine scale turbulence [2]. This simple-to-implement algebraic two-layer eddy viscosity model is based on the Cebeci–Smith method with modifications made to avoid having to locate the edge of boundary layer. A Prandtl–Van Driest formulation is used in the inner region and the Clauser formulation with Klebanoff intermittence function is used in the outer region. The Clauser, Klebanoff and other constants are adjusted to ensure that the non-dimensional normal distance from the wall y^+ encompasses the boundary layer. Typically, with the help of clustering, about 20 grids are ensured in the boundary layer. No attempt has been made to monitor explicitly the level of turbulence. The physical domain is mapped into a rectangular computational domain and all the computations are performed on transformed domains. Governing equations in the transformed co-ordinate system (ξ, η) are given below

$$\frac{\partial \bar{U}}{\partial t} + \frac{\partial \bar{F}}{\partial \xi} + \frac{\partial \bar{G}}{\partial \eta} + \bar{H} = 0$$

where

$$\bar{U} = \frac{U}{J}, \qquad \bar{F} = \frac{(\xi_x F + \xi_y G)}{J}, \qquad \bar{G} = \frac{(\eta_x F + \eta_y G)}{J}, \qquad \bar{H} = \frac{H}{J}$$

and J is the Jacobian of transformation defined as $J = (\xi_x \eta_y - \xi_y \eta_x)$.

Similarly the viscous shear stresses and heat fluxes in the transformed co-ordinate system are computed using the following relations:

$$\frac{\partial u}{\partial x} = \xi_x u_\xi + \eta_x u_\eta, \qquad \frac{\partial u}{\partial y} = \xi_y u_\xi + \eta_y u_\eta$$

$$\frac{\partial v}{\partial x} = \xi_x v_\xi + \eta_x v_\eta, \qquad \frac{\partial v}{\partial y} = \xi_y v_\xi + \eta_y v_\eta$$

$$\frac{\partial T}{\partial x} = \xi_x T_\xi + \eta_x T_\eta, \qquad \frac{\partial T}{\partial y} = \xi_y T_\xi + \eta_y T_\eta$$

These governing equations are solved by the explicit, finite difference scheme of MacCormack [3]. This predictor–corrector scheme is second-order accurate both in space and time and is easy to implement

$$\overline{U_{i,j}^{n+1}} = U_{i,j}^{n} - \frac{\Delta t}{\Delta x}\,(E_{i+1,j}^{n} - E_{i,j}^{n}) - \frac{\Delta t}{\Delta y}\,(F_{i,j+1}^{n} - F_{i,j}^{n})$$

$$U_{i,j}^{n+1} = \frac{1}{2}\left[U_{i,j}^{n} + \overline{U_{i,j}^{n+1}} - \frac{\Delta t}{\Delta x}\,(\overline{E_{i,j}^{n+1}} - \overline{E_{i-1,j}^{n+1}}) - \frac{\Delta t}{\Delta y}\,(\overline{F_{i,j}^{n+1}} - \overline{F_{i,j-1}^{n+1}}) \right]$$

In the above scheme, forward differences are used for all spatial derivatives in the predictor step, while backward differences are used in the corrector step. The forward and backward differences are alternated between predictor and corrector step, as well as between the spatial derivatives in a sequential fashion. This eliminates any bias due to the one-sided difference. For high-Reynolds number flows, the viscous regions become very thin and hence the mesh is highly refined to accurately resolve the viscous boundary layer flow. Simple algebraic grids are used for computations. Additionally, a one-dimensional stretching function is used for distributing points in a particular zone so these specific regions of the computational domain can be resolved accurately. For the viscous flow through air intakes it would be appropriate to introduce a one-dimensional stretching function to cluster the grid points close to the wall in order to resolve the high flow gradients in that area. A stretching function of Roberts [4], later modified by Eiseman [5], is used for this purpose and is given by the following function:

$$s = P\eta^* + (1 - P)\left\{1 - \frac{\tanh[Q(1 - \eta^*)]}{\tanh(Q)}\right\}$$

P and Q are parameters that provide grid point control. P effectively provides the slope of the distribution; Q is called a damping factor by Eiseman and controls the departure from linearity. Small values of Q cause small departures. However, if P is close to unity, a departure from linearity is small and will occur only for η^* close to unity. In an explicit finite difference scheme, numerical oscillations may sometime persist as a result of inadequate mesh refinement in regions of large gradients and the solution may collapse. However, in many cases it is impractical to refine the mesh in these regions, particularly if they are away from the region of interest and are not known *a priori*. For such situations and for flow fields with discontinuities such as shocks, an artificial viscosity term is added to the Navier–Stokes equations for stabilizing the calculations. In the present study, what has been termed by 'Hung–MacCormack', as the product of fourth-order dissipation terms, with C_x and C_y as adjustable constants, is employed [6]. It is in the form of addition to the right-hand side of the predictor and corrector equations of x and y operators and is given as

$$\Delta U_{i,j} = C_x \frac{|p_{i+1,j} - 2p_{i,j} + p_{i-1,j}|(U_{i+1,j} - 2U_{i,j} + U_{i-1,j})(|u_{i,j}| + a_{i,j})\Delta t}{(p_{i+1,j} + 2p_{i,j} + p_{i-1,j})\Delta x}$$

$$\Delta U_{ij} = C_y \frac{|p_{i,j+1} - 2p_{i,j} + p_{i,j-1}|(U_{1,j+1} - 2U_{i,j} + U_{i,j-1})(|v_{i,j}| + a_{i,j})\Delta t}{(p_{i,j+1} + 2p_{i,j} + p_{1,j-1})\Delta y}$$

4. RESULTS AND DISCUSSION

4.1. Two-dimensional scramjet inlet

Two-dimensional scramjet inlet geometry experimentally studied by Yanta *et al.* [7] is considered for the present numerical investigation and is shown in Figure 1(a). The inlet is an inward turning scoop with a forebody wedge angle of 10° to achieve pre-compression to the flow entering the inlet. The leading edge of the cowl provides a 10° additional compression followed by a 13° turning.

Yanta's experiments were for three different flow conditions: one with boundary layer bleed, one without bleed and one without tripping. For the present study only flow without boundary layer bleed and without tripping condition is considered. An inlet free-stream Mach number of 4, pressure of 101.35 kN m^{-2} and temperature of 311 K were prescribed. Lower wall static pressures were experimentally measured. Adiabatic, no-slip solid-wall boundary and centreline axis of symmetry conditions were ensured. At the exit, either prescribed pressure or extrapolated boundary was ascertained for sub- and supersonic flow respectively.

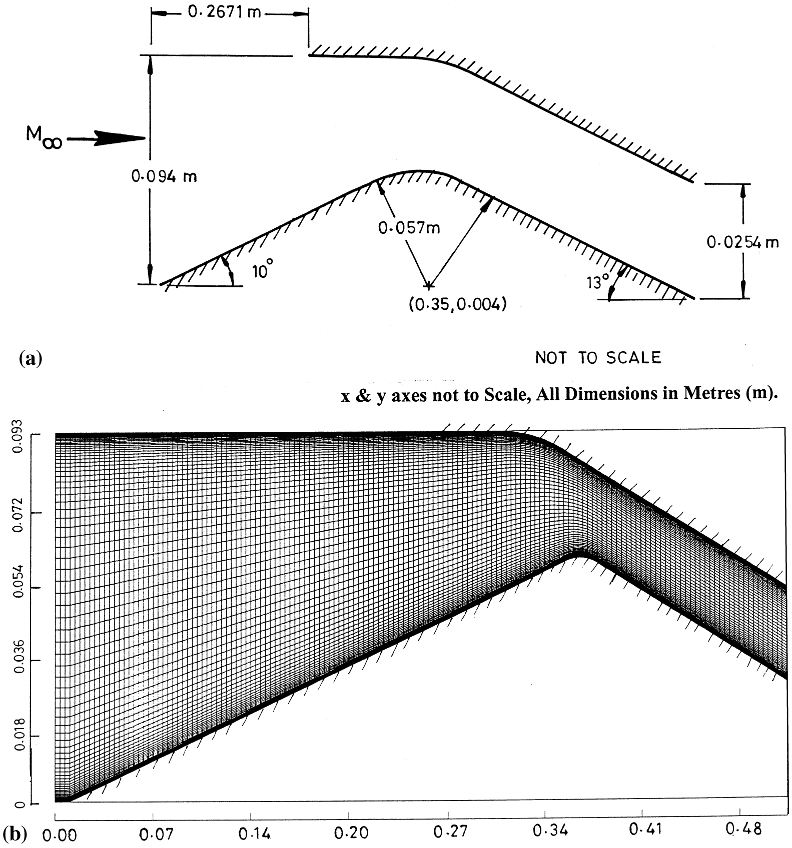

Figure 1. (a) Scramjet inlet geometry (Yanta *et al.* [7]); (b) scramjet inlet grid (151 × 91 clustered).

Initially grid-independent studies were conducted to decide about optimum grid size. Although the code uses double precision accuracy, from the computation time restrictions, a grid of 151 × 91 was found to be adequate. With a 151 × 91 *uniform grid*, numerical results predicted pressures in the duct region, which are slightly less than the experimental observations. However, for the same 151 × 91 grid but with clustering near the wall region, wall pressure distribution fell within 5 per cent of the experimental results. In the present analysis, computations are performed for Yanta's experimental inlet conditions. A clustered 151 × 91 grid is used as the baseline configuration. Figure 1(b) shows this clustered grid for two-dimensional scramjet inlet geometry. Figure 2 shows the isoMach contours for this configuration. Flow goes through the pre-compression shock due to the forebody and enters the inlet with pre-compression. The shock due to the cowl impinges onto the lower wall and gets reflected in the duct region. The shock impingement on the lower wall causes the pressure to rise. Flow passes through the multiple reflected shocks, as seen in Figure 2, in the duct before

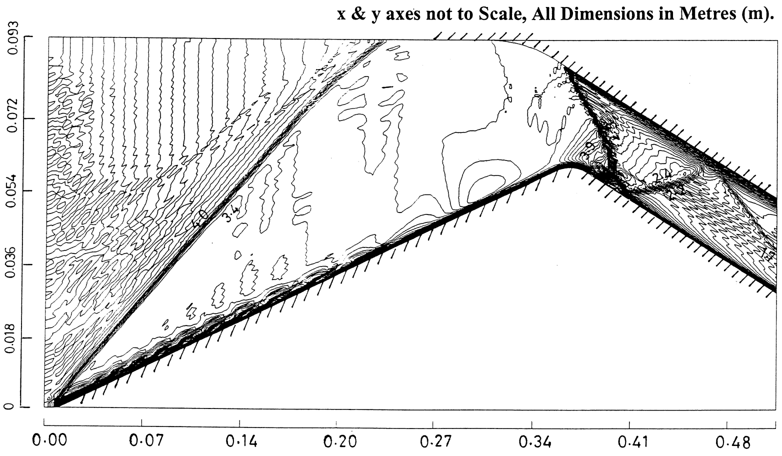

Figure 2. IsoMach contours for scramjet inlet ($M = 4$).

exiting with supersonic speeds. This adverse pressure gradient causes the flow to separate near the inlet region as seen from the velocity vector plot shown in Figure 3(a). The enlarged velocity vector field near the inlet separation region is shown in Figure 3(b).

4.2. Parametric study

After initial validation of the numerical simulation with the available experimental data, a parametric study was carried out for the same geometry with different inlet Mach numbers. Inlet Mach numbers of 3.0 and 2.5 are considered for the present study. Figure 4 shows the isoMach number contours for $M = 3.0$ inlet condition. The velocity vector field is shown in the Figure 5(a) and the enlarged view of the velocity vector field is shown in the Figure 5(b). Numerical results for another inlet Mach number ($M = 2.5$) is presented in Figure 6 in the form of isoMach number contours. Velocity vector field is shown in Figure 7(a) and an enlarged view of the velocity vector field is shown in Figure 7(b). In the absence of multiple reflected shocks in the duct region and the shock–boundary layer interaction, there is no prominent flow reversal observed in both these cases. Large flow turning from the cowl into the duct affects the velocity around the throat.

It can be observed from the isoMach contour plots that for inlet Mach numbers 3.0 and 2.5 respectively flow in the duct portion is shock free as only isentropic compression takes place followed by compression due to cowl shock impinging on the lower wall. Shock angle, pressure recovery and mass flow rate per unit width are calculated for inlet Mach numbers 3.0 and 2.5. Shock angles agreed well with calculated values using the analytical one-dimensional oblique shock theory. All the above quantities are shown in Table I. Lower wall pressure distribution compared well with experimental results of Yanta *et al.* [7], as seen in Figure 8.

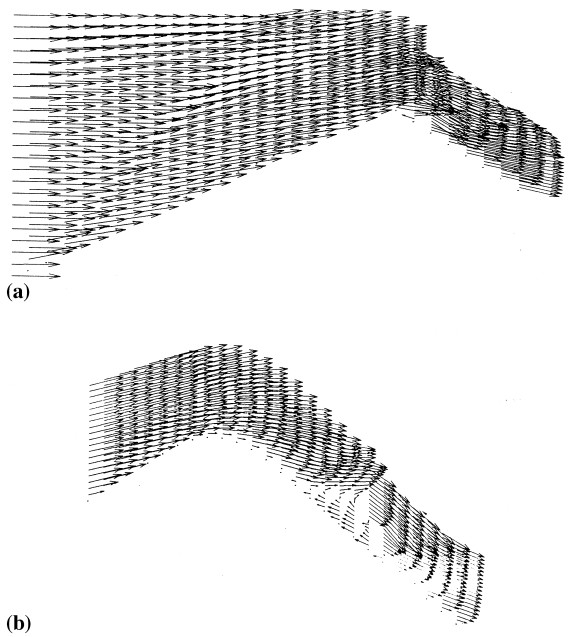

Figure 3. (a) Velocity vectors for scramjet inlet ($M = 4$); (b) enlarged view of velocity vectors ($M = 4$).

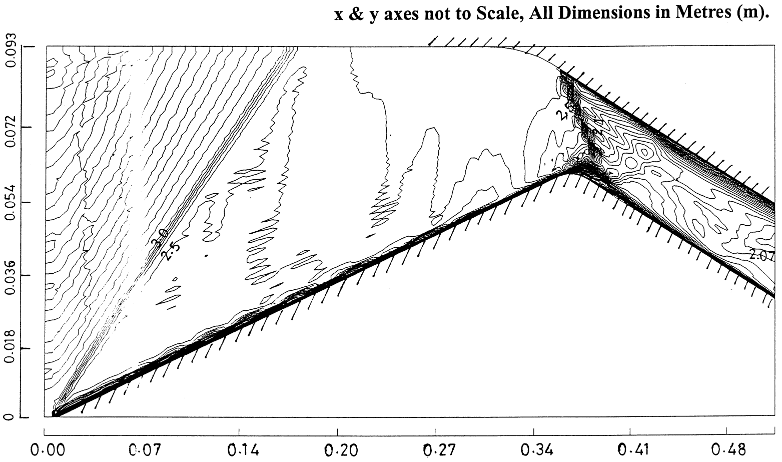

Figure 4. IsoMach contours for scramjet inlet ($M = 3$).

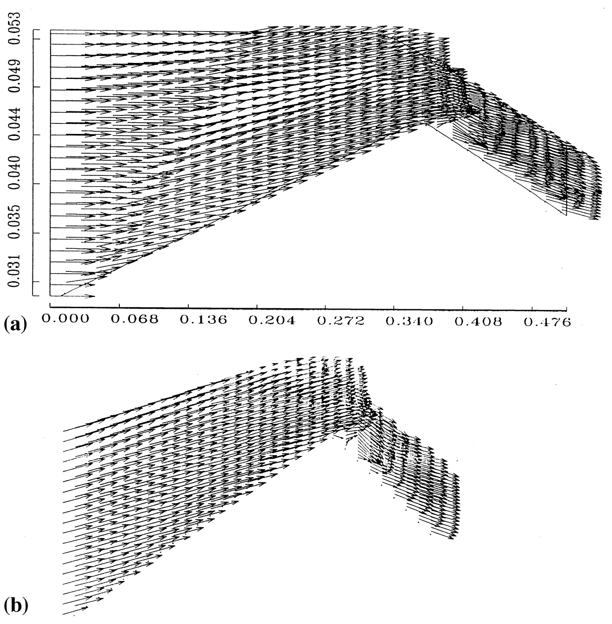

Figure 5. (a) Velocity vectors for scramjet inlet ($M = 3$); (b) enlarged view of velocity vectors ($M = 3$).

x & y axes not to Scale, All Dimensions in Metres (m).

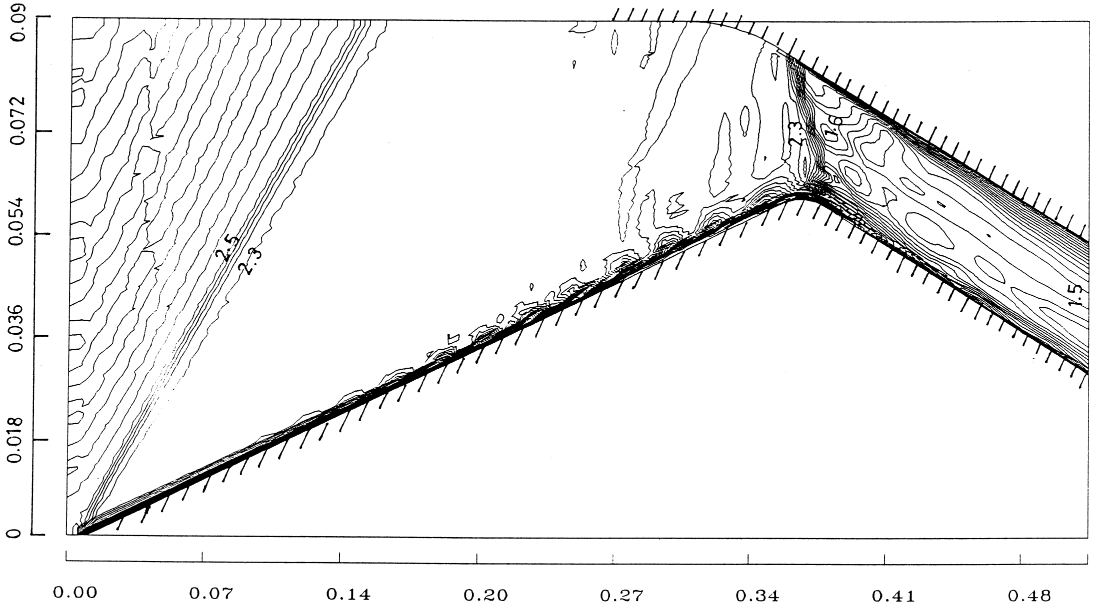

Figure 6. IsoMach contours for scramjet inlet ($M = 2.5$).

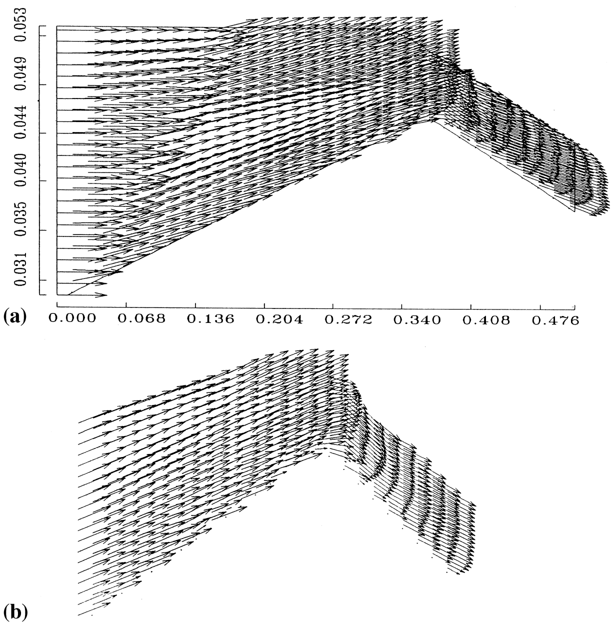

Figure 7. (a) Velocity vectors for scramjet inlet ($M = 2.5$); (b) enlarged view of velocity vectors ($M = 2.5$).

Table I. Flow parameters for flow through scramjet inlet ($p_{t0} = 0.1013$ MPa, $T_{t0} = 311$ K).

Mach number	Shock angle (°)	Pressure recovery	Mass flow rate ($\mathrm{kg\,s^{-1}\,m^{-1}}$)
4.0	23.6	0.65	5.02
3.0	28.9	0.82	2.44
2.5	33.5	0.77	2.1

4.3. Axisymmetric ramjet inlet

The axisymmetric ramjet inlet geometry experimentally investigated by Nagarathinam *et al.* [8] is considered for numerical simulation. The geometric details of the axisymmetric spike-type air intake are shown in Figure 9. It consists of straight cowl with a diameter of 50 mm, an inlet spike followed by a constant area throat at the rear. The half angle of the inlet spike is 20°. All dimensions of the geometry are given in terms of inlet constant diameter.

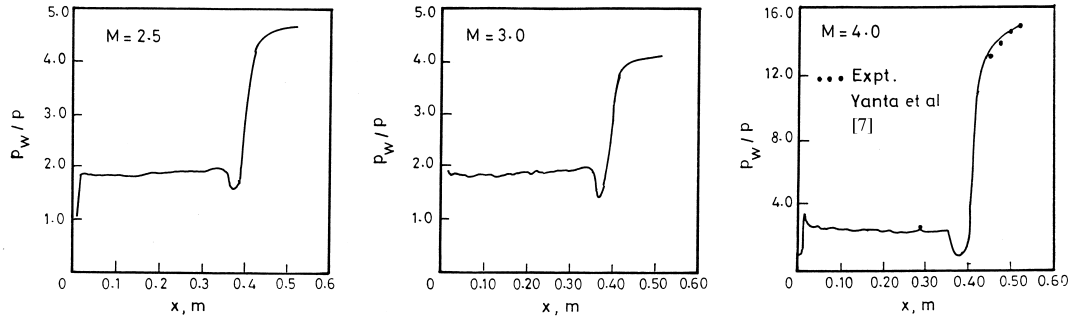

Figure 8. Wall pressure for scramjet inlet (151 × 91 clustered grid). Mach number sensitivity.

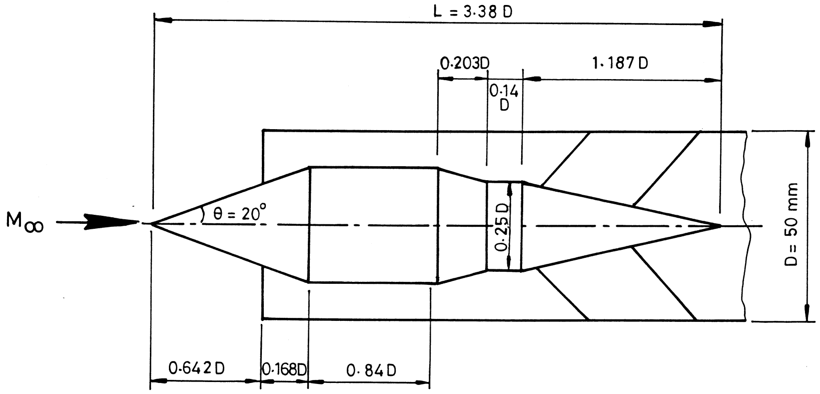

Figure 9. Axisymmetric ramjet inlet (Nagarathinam *et al.* [8]).

4.4. *Inlet flow analysis*

The inlet flow conditions in the experimental investigation mentioned above are Mach number 2.18, stagnation pressure 296 kN m^{-2} and stagnation temperature of 300 K. For the numerical simulation, at the subsonic exit initially uniform fixed static pressure is prescribed. A clustered (151 × 91) grid is selected after conducting a grid-independent study. Initially, flow encounters the compression shock due to the spike ahead of the inlet and subsequently undergoes compression. Supersonic flow entering the inlet decelerates further after passing through the reflection shock from the cowl. Normal shock is formed in the constant area throat and flow becomes subsonic behind the normal shock. Subsonic flow is further decelerated in the diverging portion. IsoMach number contours are shown in the Figure 10. All the flow features, such as leading edge shock, reflection shock and the normal shock in the throat, are well predicted. Pressure distribution on the cowl is shown in Figure 11, along with the experimental

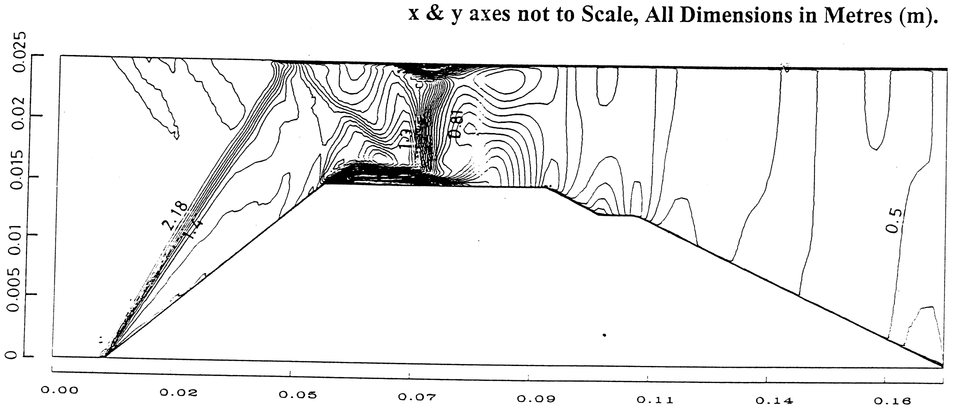

Figure 10. IsoMach contours for ramjet inlet ($M = 2.18$).

results. It is observed from the pressure distribution on the cowl in Figure 11 that, in the supersonic region, wall pressures are predicted well and the pressure rise due to the normal shock is higher than the experimentally predicted values for uniform fixed static pressure prescribed at the exit boundary. Instead, non-uniform pressure extrapolated from the interior points in the diverging portion is used as the exit pressure boundary. Results with the non-uniform extrapolated pressure profile agreed well with the experimental values and thus were used in subsequent studies. This simple method of extrapolation is commonly used for supersonic exits. However, it was observed that it is equally effective even for mixed exhaust boundary conditions. The velocity vector plot of the flow field is shown in the Figure 12(a) and the blown-up region near the inlet is also shown in Figure 12(b). It is interesting to note the presence of a double bubble from the upper wall and the centrebody forming an aerodynamic throat. This causes a normal shock at this location decelerating the flow to subsonic speeds.

4.5. Parametric study

Numerical investigation on the ramjet inlet geometry is carried out for different inlet flow conditions namely for different inlet Mach numbers and for different central spike positions relative to the cowl. Inlet flow Mach numbers of 3.0 and 1.5 are considered without any change in the spike position. The effect of spike position on the inlet flow field is also studied by moving the spike 5 mm inwards and outwards of the cowl. Stagnation pressure and temperature are kept constant at 296 kN m^{-2} and 300 K respectively for all the above four different inlet conditions.

Figure 13 shows isoMach contours of the $M = 3.0$ flow. From this figure it can be observed that the shock impingement point on the cowl is moved inside. The terminal shock position in the throat is also moved further down. Because of the high adverse pressure gradient across the normal shock, boundary layer separation occurs in the throat region before the normal shock. Velocity vector field is shown in Figure 14(a) and the enlarged view near the throat with the boundary layer separation region is shown in Figure 14(b).

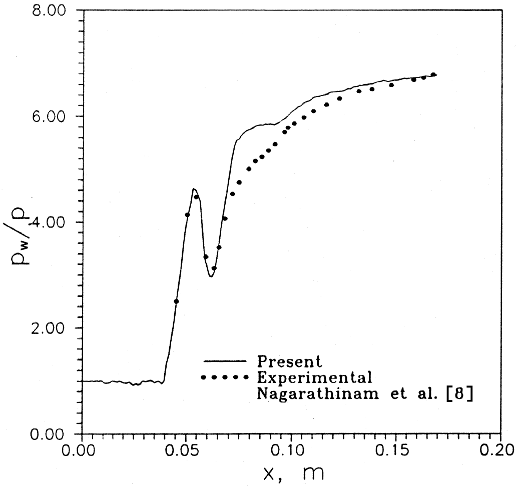

Figure 11. Wall pressure for ramjet ($M = 2.18$, uniform exit pressure).

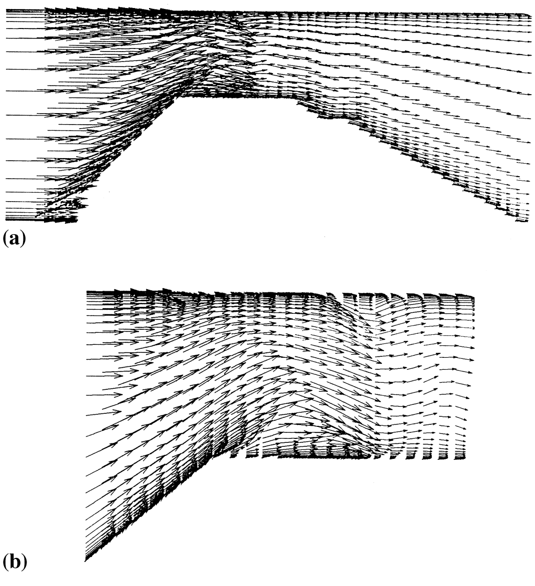

Figure 12. (a) Velocity vectors for ramjet inlet ($M = 2.18$); (b) enlarged view of velocity vectors ($M = 2.18$).

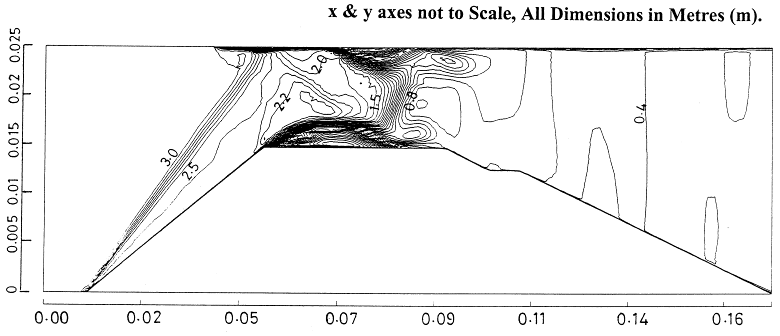

Figure 13. IsoMach contours for ramjet inlet ($M = 3$).

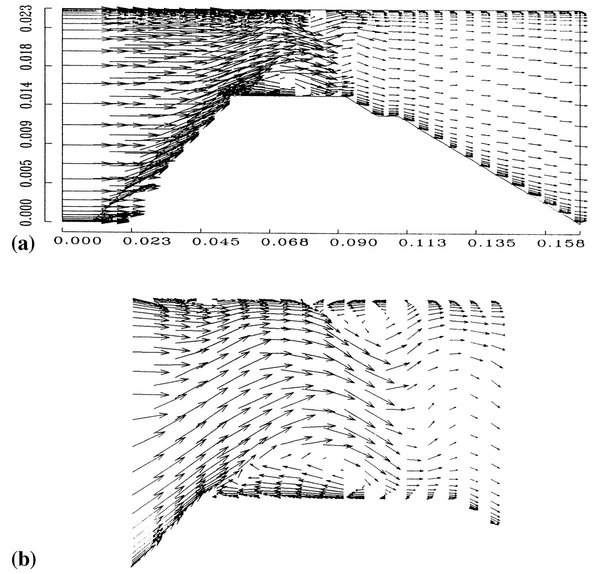

Figure 14. (a) Velocity vectors for ramjet inlet ($M = 3$); (b) enlarged view of velocity vectors ($M = 3$).

Computations are performed on the flow with inlet Mach number 1.5. IsoMach contours are shown in Figure 15. Shock induced due to the spike and normal shock moved out of the cowl and standing at the inlet can be observed in the above figure. Figure 16 shows the velocity vector field. Figure 17 shows wall pressure distribution for the three cases where Mach number variation was tried. Comparison with the experimental results is available only for the design with a Mach number of 2.18. It can be seen that the agreement with the experimentally x & y axes not to Scale, All Dimensions in Metres (m).

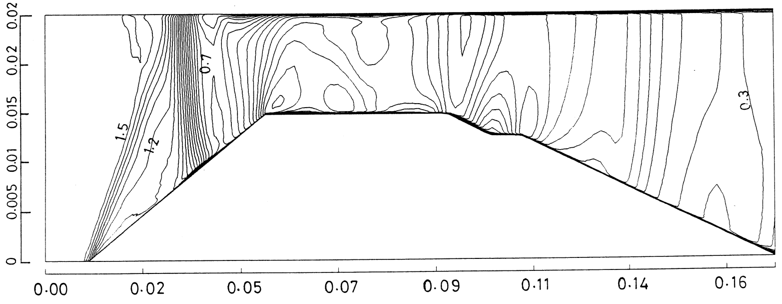

Figure 15. IsoMach contours for ramjet inlet ($M = 1.5$).

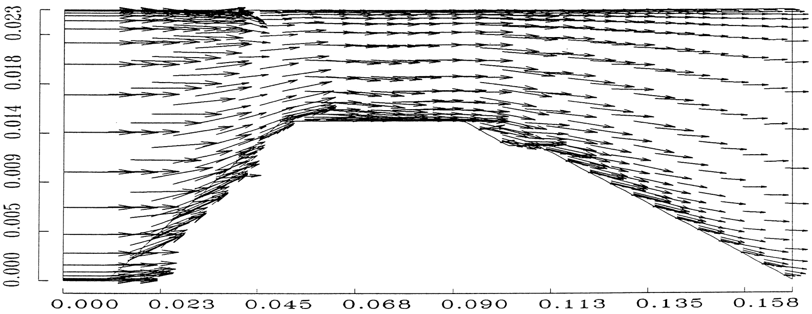

Figure 16. Velocity vectors for ramjet inlet ($M = 1.5$).

available data is very good. Mach number 3 exhibits multiple shock structure, whereas flow with Mach number 1.5 is well behaved with oblique shocks.

Figure 18 shows isoMach contours for the flow with inlet Mach number 2.18 and a 5-mm inward spike movement. It is seen from the above figure that the flow is complex with a number of oblique and reflected shocks. Double separation bubble from the top wall and the centrebody and associated throat is also clearly seen. Figure 19(a) shows the velocity vector field. It can be observed from the above figure that the flow separation takes place ahead of the normal shock on both the top and bottom solid surface due to large adverse pressure gradient. This is also clearly seen in Figure 19(b). In contrast, with the spike movement of 5 mm outwards of the cowl for the inlet Mach number 2.18, the flow pattern exhibits a lower number of shocks. Figure 20 shows the isoMach contours of the flow. It is seen from the above figure that normal shock stands outside the cowl and chokes the inlet. Subsequently, the flow after the normal shock and in the ramjet is entirely subsonic. Figure 21 shows the isobars for the above case. Figures 22 and 23 show the velocity distribution near the solid surface, on the

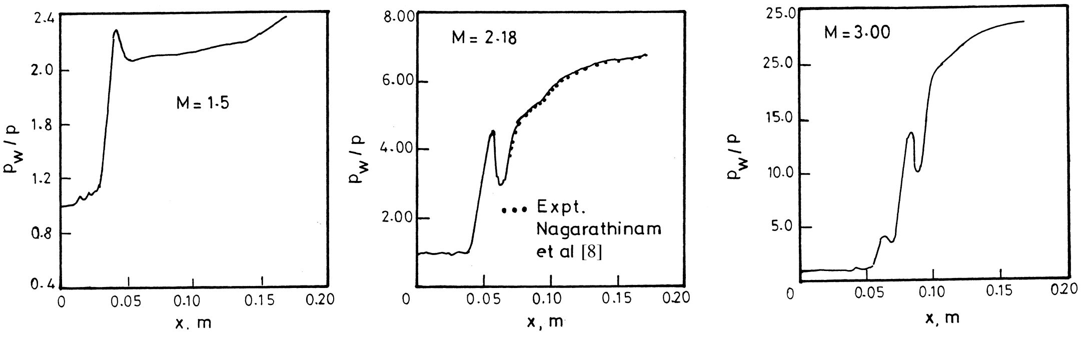

Figure 17. Wall pressure for ramjet inlet (151 × 91 clustered grid). Mach number sensitivity.

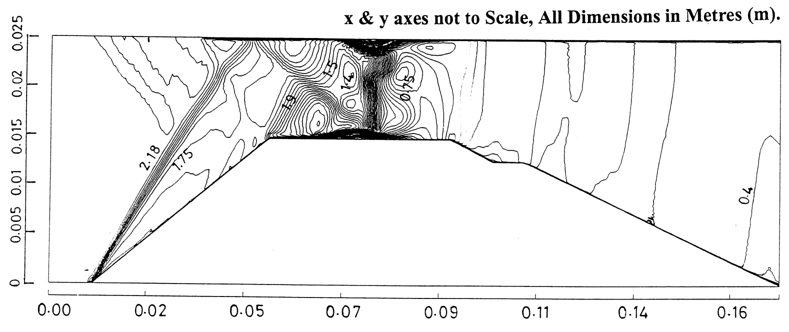
x & y axes not to Scale, All Dimensions in Metres (m).

Figure 18. IsoMach contours for ramjet inlet ($M = 2.18$, spike 5 mm inwards).

ramp as well as the straight middle portion. There is a small re-circulation region and the development of the boundary layer is amply demonstrated, which is possible to capture due to the clustered grid. Figure 24 shows wall pressure distribution for the three cases where spike movement was studied. It essentially reinforces arguments made earlier.

Typical pressure convergence history shown in Figure 25 is for a baseline case. Due to the complexity of shock–boundary layer interaction and associated separated and reattached flow structure, the pressure convergence of less than four orders of magnitude is achieved in about 3000 iterations. It may be mentioned here that the other conservative flow variables showed still better levels of convergence. A minimum of four lengthwise computational sweeps, with this prescribed value of pressure convergence, were carried out for realizing steady state solution.

For the axisymmetric spike type air intake, all the flow features are predicted well. Wall pressures are in good agreement with the experimental values and fall with in 5 per cent accuracy. Pressure recovery and mass flow rate calculated are shown in Table II. Experimental pressure recovery is 0.789 and the computed one is 0.80.

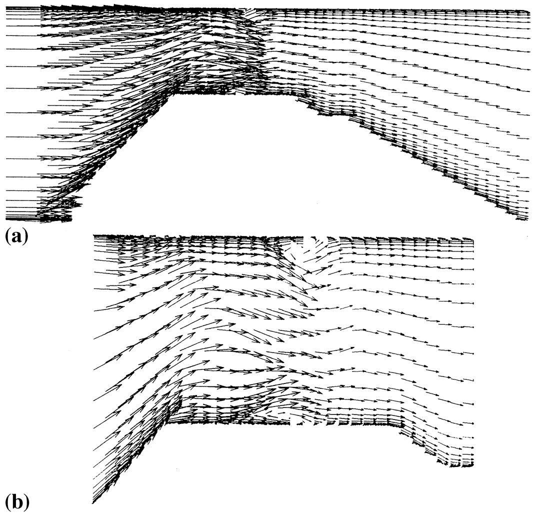

Figure 19. (a) Velocity vectors for ramjet inlet ($M = 2.18$, spike 5 mm inwards); (b) enlarged view of velocity vectors ($M = 2.18$, spike 5 mm inwards).

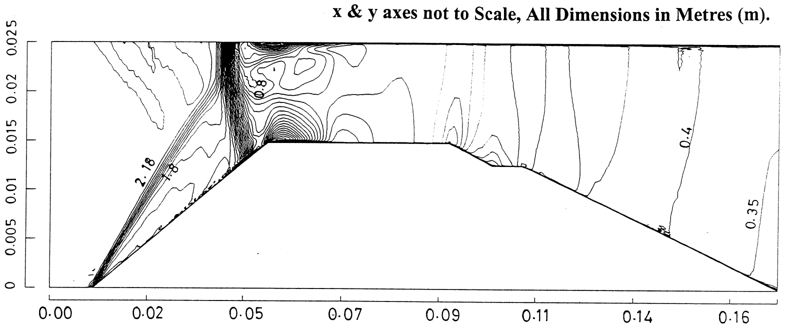

Figure 20. IsoMach contours for ramjet inlet ($M = 2.18$, spike 5 mm outwards).

5. CONCLUSIONS

The supersonic inlet performance depends on the required mass flow rate with high-pressure recovery over the complete operating range. Further, it is necessary to understand shock positions along with the flow separation regions associated with adverse pressure gradients. The code presented here is capable of predicting all the complex inlet flow features, such as the shock due to forebody, multiple shock reflections, normal shock, shock–boundary layer interaction and associated separation for two-dimensional and axisymmetric inlets. Computed

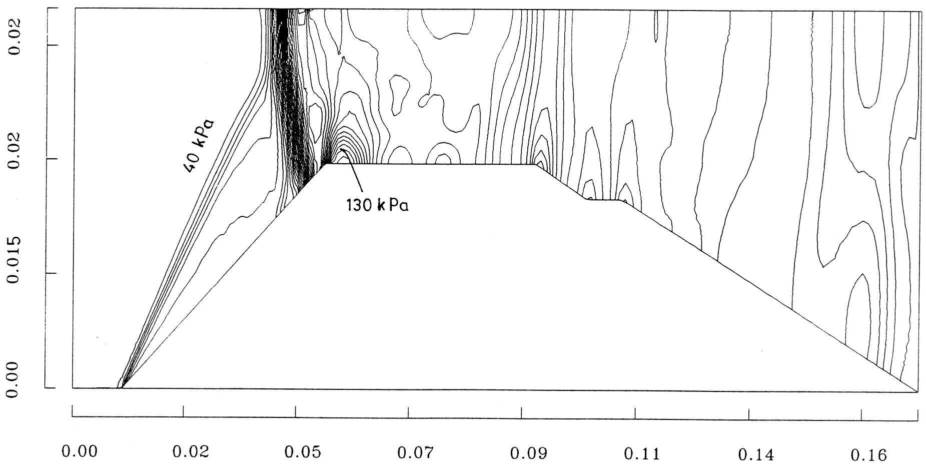

Figure 21. Isobar contours for ramjet inlet ($M = 2.18$, spike 5 mm outwards).

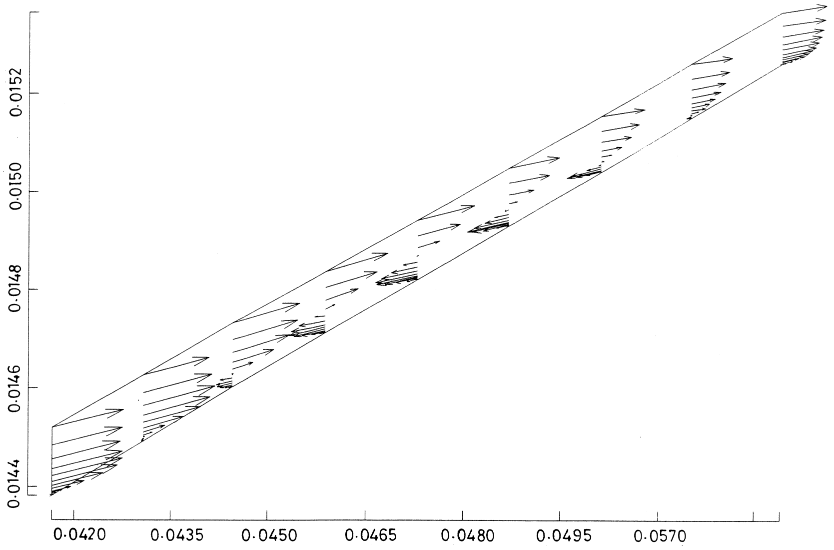

Figure 22. Enlarged view of velocity vectors on ramp ($M = 2.18$, spike 5 mm outwards).

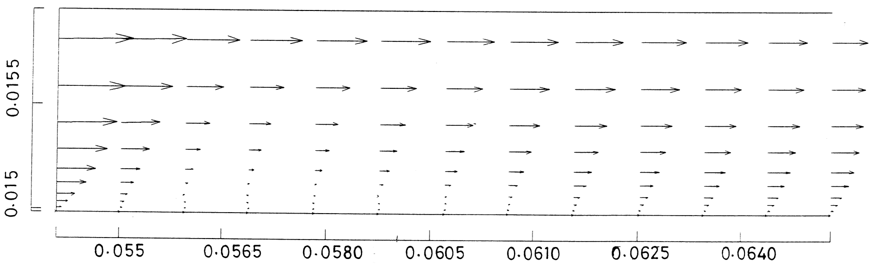

Figure 23. Enlarged view of velocity vectors on straight middle portion ($M = 2.18$, spike 5 mm outwards).

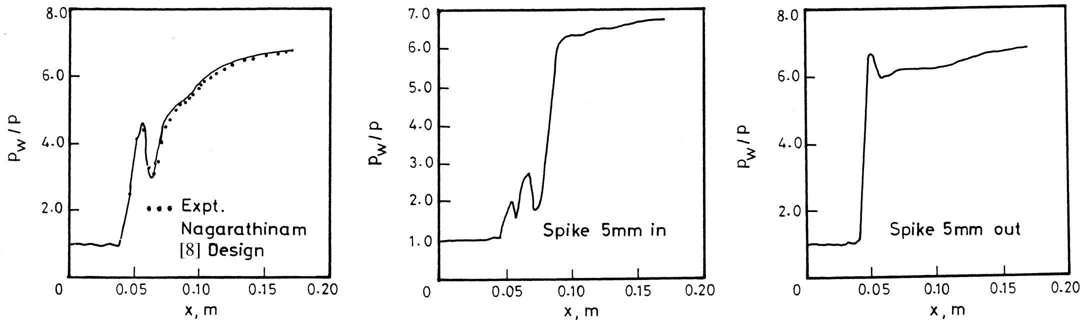

Figure 24. Wall pressure for ramjet inlet (151 × 91 clustered grid). Spike movement sensitivity.

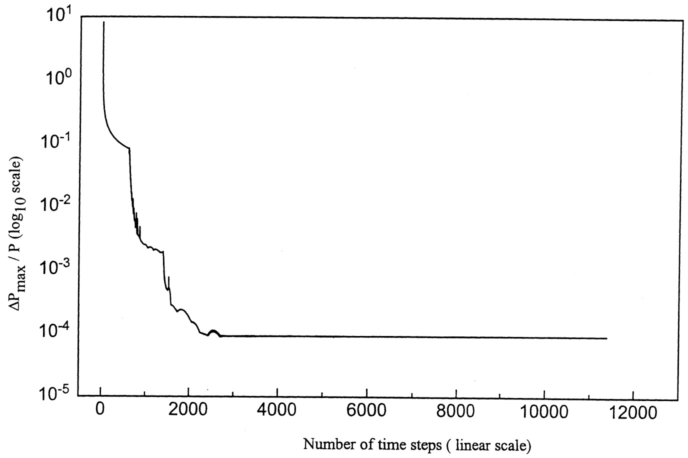

Figure 25. Typical convergence history.

Table II. Flow parameters for flow through Ramjet Inlet ($p_{t0} = 0.296$ MPa, $T_{t0} = 300$ K).

Mach number	Spike movement (mm)	Pressure recovery	Mass flow rate (kg s^{-1})
2.18	0	0.80	0.80
3.0	0	0.65	0.94
1.5	0	0.69	0.56
2.18	5 (inward)	0.70	0.73
2.18	5 (outward)	0.65	0.65

values are in good agreement with experimental data available. This code could be used to study supersonic inlet performance under off-design operating conditions.

APPENDIX A. NOMENCLATURE

a	speed of sound (m s^{-1})
c_p, c_v	specific heat at constant pressure and constant volume (J kg^{-1} K^{-1})
C_x, C_y	coefficients in the smoothing terms
e	internal energy per unit mass (J kg^{-1})
E_t	total energy per unit volume (J m^{-3})
F, G	flux vectors
H	source vector
I	0 for two-dimensional flows 1 for axisymmetric flows
k	coefficient of thermal conductivity (W m^{-1} K^{-1})
p	pressure (N m^{-1})
Pr	Prandtl number
q	heat flux vector (W m^{-2})
t	time (s)
T	temperature (K)
u	component of velocity vector in x-direction (m s^{-1})
U	vector of conservative variables
v	component of velocity in y-direction (m s^{-1})
V	velocity vector
x, y	Cartesian co-ordinates
y	radial distance (m)

Greek letters

μ	coefficient of viscosity (N s m^{-2})
ρ	density (kg m^{-3})
τ	shear stress (N m^{-2})

Δt	time step (s)
∇	divergence operator (m^{-1})

Subscripts

0	stagnation condition
i	grid location in x-direction
j	grid location in y-direction
l	laminar value
t	turbulent value
w	wall condition
x	partial differentiation with respect to x
y	partial differentiation with respect to y

Superscripts

n	time level

REFERENCES

1. Gokhale SS, Suresh R. Numerical computation of internal flows for axi-symmetric and two dimensional nozzles. *International Journal of Numerical Methods in Fluids* 1997; **24**: 599–610.
2. Baldwin B, Lomax H. Thin layer approximation and algebraic model for separated turbulent flows. AIAA Paper 78-257, 1978.
3. MacCormack RW. The effect of viscosity in hypervelocity impact cratering. AIAA Paper 69-354, 1969.
4. Roberts GO. Computational meshes for boundary layer problems. *Lecture Notes in Physics* 1971; **8**: 171–177.
5. Eiseman PR. A multi-surface method of co-ordinate generation. *Journal of Computational Physics* 1979; **33**: 118–150.
6. Hung CM, MacCormack RW. Numerical solutions of supersonic and hypersonic laminar compressible corner flows. *AIAA Journal* 1976; **14**(4): 475–481.
7. Yanta WJ, Collier AS, Spring C III, Boyd W, Christopher F, McArthur JC. Experimental measurements of the flow in a scramjet inlet at Mach 4. *Journal of Propulsion* 1990; **6**(6): 784–790.
8. Nagarathinam M, Gupta A, Davidson D. Wind tunnel testing of axisymmetric air intake. Technical Report, DRDL, 5120.1003.000, NAL, 1985.